

1  
2  
3  
4  
5  
6  
7  
8  
9  
10  
11  
12  
13  
14  
15  
16  
17  
18  
19  
20  
21  
22  
23  
24  
25  
26  
27  
28  
29  
30  
31  
32  
33  
34  
35  
36  
37  
38  
39  
40  
41  
42  
43  
44  
45  
46

**Anthropogenic Aerosols Dominate the Forced Contribution to Historical  
Precipitation Trends in Populated Regions**

Kayla White<sup>1</sup>, Geeta G. Persad<sup>1</sup>, Bjørn H. Samset<sup>2</sup>, Clara Deser<sup>3</sup>, Adam S. Phillips<sup>3</sup>, Laura J.  
Wilcox<sup>4</sup>, Marianne T. Lund<sup>2</sup>, Xueying Zhao<sup>1,3</sup>

*<sup>1</sup>Department of Earth and Planetary Sciences, The University of Texas at Austin, Austin, Texas,  
USA*

*<sup>2</sup>CICERO Center for International Climate Research, Oslo, Norway*

*<sup>3</sup>National Center for Atmospheric Research, Boulder, Colorado, USA*

*<sup>4</sup>National Centre for Atmospheric Science, University of Reading, Reading, UK*

*Corresponding author: Kayla White, [kaylaw@utexas.edu](mailto:kaylaw@utexas.edu)*

47 **Abstract**

48  
49       Constraining the relative role of anthropogenic aerosols (AERs) and greenhouse gases  
50 (GHGs) -- the primary drivers of anthropogenic climate change -- in historical global  
51 precipitation change is critical to accurately anticipating near-term impacts. However, internal  
52 variability and model disagreement in global-scale attribution have made identifying the  
53 regionally evolving impacts of AERs and GHGs on recent precipitation shifts and their  
54 associated, substantial societal impacts challenging. Here, we investigate the relative influence of  
55 AERs and GHGs on evolving 50-year historical terrestrial precipitation trends using simulations  
56 from the CMIP6 Large Ensemble Single Forcing Model Intercomparison Project. We find that  
57 AERs and GHGs each govern forced historical precipitation trends in different regions and time  
58 periods, but that AERs dominate trends in most populated regions over much of the historical  
59 period. AERs dominate terrestrial precipitation trends from 1930-1979 over most areas, driven  
60 mainly by circulation-induced effects from North American and European emissions. The  
61 subsequent geographic shift in AER emissions from these regions to Asia drives AER dominance  
62 of summertime precipitation trends from 1950-1999 and 1970-2019 over populous regions  
63 globally. AERs' leading influence on forced historical precipitation trends is reflected in their  
64 high but time-varying apparent hydrologic sensitivity, contrary to GHG dominance of  
65 temperature trends. The spatiotemporal variability and overall primacy of AERs' role in forced  
66 historical precipitation trends demonstrates that extrapolating past precipitation shifts to predict  
67 future impacts could misrepresent future global and regional hydrologic change in the face of  
68 rapid AER emission changes and highlights the importance of constraining near-future AER  
69 emissions uncertainty.

70  
71  
72 **Significance Statement**

73  
74       Diverse model representations of the response of precipitation to spatiotemporally  
75 variable anthropogenic aerosol and uniform well-mixed greenhouse gases have made  
76 understanding regional drivers of forced precipitation change over the historical period difficult.  
77 Using a multi-model large ensemble dataset that accounts for structural uncertainty and internal  
78 variability, we robustly identify how the differing spatial patterns, radiative properties, and  
79 temporal evolution of anthropogenic aerosols and greenhouse gases impact forced precipitation  
80 trends. We find anthropogenic aerosol changes dominate forced precipitation trends over  
81 populated regions, making them a key consideration in regional climate risk assessments.

82  
83  
84 **I. Introduction**

85  
86       Anthropogenic aerosols (AERs) and greenhouse gases (GHGs) have co-evolved over the  
87 industrial era, but differ substantially in behavior and impacts (1–3). AERs impose a net cooling  
88 via direct scattering of shortwave radiation and interactions with clouds, offsetting approximately  
89 one-third of the net global warming caused by well-mixed GHG absorption of longwave  
90 radiation (4, 5). AERs have a relatively short lifetime of days to weeks in the troposphere (4, 6),  
91 leading to atmospheric concentrations near or downwind of emission sources and industrialized  
92 regions. This nonuniform AER distribution leads to temporal and spatial heterogeneity in both

93 the radiative forcing of AERs and their atmospheric effects throughout the historical period (2, 4,  
94 7–12). By contrast, long-lived GHGs have increased monotonically with an intensifying but  
95 largely static spatial pattern of climate influence, resulting in a steady increase in global-mean  
96 temperature (3). These differing qualities of the prominent anthropogenic forcings have led to  
97 significant discrepancies in the representation of human-induced climate change, detection and  
98 attribution of forcing-driven impacts, and model projections.

99  
100 The nonuniform behavior of AER emissions associated with the shifting geography of major  
101 emitters has led to significant decadal shifts in the distribution and magnitude of radiative forcing  
102 throughout the recent historical period, seen clearly in the evolving distribution of aerosol optical  
103 depth (AOD) (Figure 1a-c). In the early 20th century, sulfate emissions over North America and  
104 Europe increased from 1920 to 1975 (steeply from 1955 to 1975; (2, 13)), resulting in large-scale  
105 Northern Hemispheric (NH) cooling, an increasing interhemispheric temperature gradient, and a  
106 resulting southward shift of the Intertropical Convergence Zone (ITCZ) (14–17). Increasing  
107 AOD not only reduced NH precipitation overall but produced regional impacts such as the  
108 drying of the Sahel (15, 18, 19) and weakening of the West African (20) and South Asian (21)  
109 monsoons, detectable beyond internal variability (22, 23). An increase in tropical biomass  
110 burning aerosol emissions from 1945 to 1990 (2) coincidentally produced a similar spatial  
111 distribution of AER radiative forcing as GHGs but with opposite sign. This transition, combined  
112 with declining North American and European AOD, resulted in the offset of many GHG-driven  
113 effects (24, 25). Subsequently, steadily increasing AOD over South and East Asia offset the  
114 pronounced declines in North American and European sulfate emissions since 1975, resulting in  
115 continued East and South Asian monsoon suppression (23, 26) with only recent remotely driven  
116 recovery observed in South Asia (27), and a recovery of Sahel rainfall (14) as GHG-driven  
117 warming intensified. This spatiotemporally evolving AER distribution strongly impacted the  
118 strength with which AERs offset GHG-driven climate changes in different regions and time  
119 periods (2, 8, 24, 28), an effect which is obscured by global-mean or historical-mean assessments  
120 of precipitation drivers (29–31).

121  
122 AERs and the ratio of aerosol species impact global and regional precipitation through  
123 different forcing-driven (fast) and temperature-mediated (slow) mechanisms, which differ from  
124 those of GHGs (32–35). Purely shortwave scattering aerosol species, such as sulfate, reduce  
125 global temperature, as top-of-atmosphere outgoing radiative flux and surface flux decrease at the  
126 same rate (36). Much of the reduction in surface insolation is balanced by a reduction in surface  
127 evaporation (i.e., slow response) which thereby suppresses precipitation and slows the  
128 hydrological cycle (33, 37). Absorbing aerosol species, such as black carbon, reduce reflected  
129 top-of-atmosphere solar flux and the incident surface solar flux, increasing atmospheric  
130 temperature, and suppressing precipitation through convective inhibition (i.e., fast response;  
131 (32). However, black carbon can enhance precipitation in the long-term temperature-mediated  
132 response, as it eventually results in surface warming (36, 38). In situ, the radiative effect of  
133 atmospheric aerosol will have differing implications on precipitation response depending on the  
134 vertical profile and mix of AER species (39–41), and the climatological drivers in that region  
135 (33, 36, 42). Furthermore, the location of emissions relative to regions controlling large-scale  
136 circulation can lead to remote perturbations in precipitation (18, 43–46). As a result, total AER-  
137 driven precipitation change is a combination of the fast and slow responses induced by regionally

138 and vertically diverse AER species, although the slow response has a more substantial  
139 contribution to multidecadal historical and near-future impacts of AERs on the hydrologic cycle  
140 in most regions (34, 36). In contrast, well-mixed GHGs trap longwave radiation, which increases  
141 atmospheric temperature, evaporation, and atmospheric water vapor content globally (5).  
142 However, energetic constraints result in increased precipitation at specific latitudinal or  
143 geographical locations, contributing to wetting in climatologically wet regions and drying in arid  
144 regions (i.e., “wet-get-wetter, dry-get-drier” or “warmer-get-wetter” paradigms; (1, 47–49).  
145 Thus, the hydrologic response to AERs is not a scalable offset to GHGs, and the resulting  
146 hydrologic change from AERs and GHGs can regionally compound or counteract depending on  
147 the timescale, regional climatology, and location relative to emissions.  
148

149 The complex interplay of the dominant anthropogenic forcings has made robustly detecting  
150 AER effects on regional precipitation challenging in the face of model structural uncertainty,  
151 climatological biases, and internal and interannual variability (47). Furthermore, it can be  
152 difficult to distinguish the time-evolving response to GHGs and AERs (especially AERs on  
153 decadal timescales) from modes of natural variability (31, 50–53). There have been several  
154 studies that show AER have had a detectable influence on large-scale (14–16, 28, 54) and  
155 regional-scale (19–21, 55, 56) precipitation throughout the 20th century and that their impacts  
156 can often outweigh those of GHGs (32, 57, 58). However, certain methodological limitations can  
157 hinder the detectability of AER-driven effects on hydroclimate. Single-model studies can be  
158 prone to individual model biases in regional climatology and dynamical responses to  
159 anthropogenic forcings on interannual or decadal timescales. Small ensemble sizes can hinder  
160 the detectability of a forced signal amidst the noise of internal variability (59). Regional studies  
161 may overlook the influence of large-scale circulation patterns or remote teleconnections. The  
162 uncertainty in AER forcing (5) and the differing magnitude of AER-driven precipitation  
163 responses across individual GCMs (22, 32, 47, 60) further limits the accuracy of the  
164 anthropogenically-forced precipitation signal in any of these scenarios.  
165

166 Given the magnitude of detected hydroclimate shifts and associated societal damages to date,  
167 methodologies that overcome the limitations of structural uncertainty and internal variability to  
168 accurately estimate the contributions of AERs and GHGs to historical precipitation shifts will be  
169 critical to anticipating future hydroclimate change as both forcing agents evolve. The limited  
170 characterization of historical AER impacts on precipitation in previous studies limits certainty in  
171 how much of the historical forced signal and associated climate risks have been due to AERs  
172 versus GHGs, which is of particular concern given anticipated rapid but uncertain near-term  
173 declines in AER emissions in many regions (13, 61). However, the recent emergence of earth  
174 system multi-model single-forcing large ensemble datasets, such as those now available through  
175 the Large Ensemble Single Forcing Model Intercomparison Project (LESFMIP; (62)), allows a  
176 new ability to constrain the forced response with an unprecedented characterization of structural  
177 uncertainty and internal variability.  
178

179 Here, we identify the regional and temporal contribution of AERs to 50-year forced historical  
180 precipitation trends alongside GHGs in five CMIP6-generation LESFMIP models (CanESM5,  
181 CESM2, CNRM-CM6-1, IPSL-CM6-LR, MIROC6) with a range of 9 to 65 ensemble members  
182 for each single-forcing (AER-only, GHG-only) and historical all-forcing (ALL) scenario, making  
183 this the most comprehensive archive to date with which to address the role of AERs in historical

184 precipitation. We show that AERs drive historical precipitation trends globally in the early 20th  
185 century due to NH cooling and associated hemispheric temperature asymmetry driven by rising  
186 AOD in North America and Europe. AERs remain the dominant driver of precipitation over  
187 industrialized regions into the 21st century, driven largely by within-region rather than remote  
188 changes in AOD, despite increasing impacts from GHGs. The effects of AERs on precipitation  
189 are far more variable across space and time than those of GHGs. Furthermore, we show that  
190 AERs' dominance of precipitation is dependent on individual regions' climatology, local  
191 emission changes, and the reinforcement or opposition of GHG-driven precipitation trends.  
192 Although GHGs dominate historical global-mean temperature change, we demonstrate that  
193 AERs play a leading role in regional and global hydroclimate change throughout the historical  
194 period. Our results highlight the importance of constraining future AER emissions uncertainty to  
195 better anticipate controls on precipitation change in the coming decades.

## 196 197 198 **II. Results and Discussion** 199

### 200 **AER dominance of regional precipitation trends through diverse mechanistic pathways.**

201 As noted earlier, AERs and GHGs impact in situ and remote precipitation through differing  
202 thermodynamic and dynamic pathways. Hence, the mechanisms behind AER-driven  
203 precipitation change are diverse across regions and are not simply a mirror of the response to  
204 changes from GHGs. In Figure 1, we show AOD trends from 1930 to 1979 (Figure 1a), 1950 to  
205 1999 (Figure 1b), and 1970 to 2019 (Figure 1c) (referred to as the early, middle, and late trend  
206 periods, respectively), which highlight three prominent shifts in the AER distribution. The center  
207 panel (Figure 1d) shows a recent trend from 1995 to 2014 of Community Emissions Data System  
208 (CEDS) SO<sub>2</sub> emissions (63), covering a large portion of the late period, highlighting the weak  
209 correlation between trends in AER emissions and AER-driven precipitation. In surrounding  
210 panels (Figure 1e-1j), we show how AERs (blue bar), GHGs (green bar), ALL (black circle), and  
211 linearly added AER+GHG (red square) drive June-August (JJA) precipitation trends across these  
212 three periods. We show select populated regions in order to explore the hydroclimate response to  
213 individual anthropogenic forcings, and the additivity of the response to forcings, in areas  
214 sensitive to physical hazards. While there are variable pathways through which AERs can  
215 dominate historical precipitation trends, each with unique implications for regional detection and  
216 attribution, hazard analysis, and future anthropogenic impacts, we focus on two prominent AER-  
217 driven pathways here: remote circulation-driven and local radiatively-driven pathways.

218  
219 Regional aerosol emission changes can drive precipitation change far from emission sources  
220 through long-range transport of the aerosols themselves or energetic communication through  
221 large-scale circulation responses and associated teleconnections (18, 33, 43–46) This latter  
222 remote mechanism underlies the impact of North American and European AOD (Figure 1a) on  
223 Saharan (SAH) and West African (WAF) precipitation (Figure 1h, 1i). In WAF and SAH, rising  
224 North American and European AOD induce remote spatial-mean drying in the early period  
225 (Figure 1h, 1i) due to the associated cooling of the NH, and the resulting southward shift of the  
226 tropical rainbelt (15, 18, 19). Conversely, decreasing North American and European and rising  
227 Asian AOD in the late period (Figure 1c) cause spatial-mean wetting in WAF and SAH (Figure  
228 1h, 1i) through combined ocean-mediated and direct atmospheric processes (64, 65). This  
229 meridional transition of AOD trends between the middle and late period decreases hemispheric

230 temperature asymmetry (14), resulting in a northward shift of the ITCZ (19, 66), which surpasses  
231 the additional wetting from rising GHGs (Figure 1h, 1i). This exemplifies conditions under  
232 which historical AER-dominance can arise via remote circulation-driven responses,  
233 demonstrating AERs' far-reaching impacts relative to emission location.

234  
235 It is well-established that AOD increases drive localized drying by suppressing surface  
236 energy fluxes and increasing atmospheric absorption (33, 37, 67, 68); however, the magnitude of  
237 these in situ precipitation impacts relative to local AOD trends and their ability to overcome  
238 GHG-driven effects can differ dramatically depending on region-specific drivers of  
239 climatological precipitation, and on the balance between absorbing and scattering aerosol  
240 species. These locally driven, but variable precipitation responses to regional AOD changes  
241 (Figure 1a, 1b, 1c) can be seen when comparing Eastern North American (ENA), South Asian  
242 (SAS), and East Asian (EAS) precipitation trends. In ENA, increasing and decreasing local AOD  
243 trends (Figure 1a, 1c) drive comparable drying and wetting in ALL in the early and late periods  
244 (Figure 1f), respectively. In contrast, in SAS, the magnitude of AER-driven drying is smallest in  
245 the late period compared to the two preceding periods (Figure 1j), despite the continual rise in  
246 local AOD and emissions throughout the historical period (Figure 1c, 1d). In EAS, the magnitude  
247 of AER-driven drying remains large in all three periods driven by increasing AOD locally, which  
248 drives the ALL precipitation response in the early period, but is cancelled by GHG-driven  
249 wetting in the late period (Figure 1k). Hence, local AOD or emissions trends may not be the sole  
250 predictor of the sign or magnitude of AER-driven hydroclimate change due to the dependence on  
251 regional climatological drivers (69, 70).

252  
253 **Aerosol dominance of absolute land precipitation trends throughout the 20th and early**  
254 **21st century.** Our preceding analysis shows that AERs can overwhelm GHG-driven  
255 precipitation change in individual regions (Figure 1e-1k). Taking a global perspective, we next  
256 apply a similar framework to identify the relative dominance by AERs and GHGs of seasonal  
257 terrestrial precipitation worldwide. To construct Figure 2, we calculate the absolute value of the  
258 precipitation trend in ALL, AER, GHG, and their residual ( $ALL - AER + GHG$ ), which captures  
259 both nonlinearities and other anthropogenic forcings such as land use change, at every grid point.  
260 We then calculate the area-weighted spatial mean of these absolute precipitation trends in AER,  
261 GHG, and the residual relative to ALL. A given forcing can produce both positive and negative  
262 signals within a specified region, each of which constitute significant changes in local  
263 precipitation, but may average to near-zero in a regional mean. Hence, by taking the absolute  
264 value of precipitation trends before the spatial mean, we preserve the strength of the signal from  
265 each forcing agent within the specified region. Where the spatial-mean of AER-induced absolute  
266 precipitation trends is greater than that of GHGs and other residual natural and/or anthropogenic  
267 forcings in that region, AER is the largest forcing contribution to ALL and we identify this as an  
268 AER-dominant region. AER dominance can occur when the AER signal overwhelms an  
269 opposing GHG effect (red) or is complemented by a weaker GHG signal of the same sign  
270 (green). Importantly, diverging (red) and unidirectional (green) signals do not indicate the sign of  
271 the precipitation trend, but rather the agreement (or disagreement) in trend direction. AER  
272 dominance can, and does, manifest as any combination of these, showing the complex variability  
273 in how AERs influence regional precipitation.

274

275 In the LESFMIP multi-model mean, we find that AERs dominate forced historical (ALL)  
276 terrestrial precipitation trends in all seasons in the mid-20th century (1930 to 1979) based on  
277 absolute magnitude (Figure 2a-2c). The extent of AER dominance of historical precipitation  
278 trends decreases through the late 20th century and turn of the 21st century (1950 to 1999 and  
279 1970 to 2019 periods, Figure 2d-2i), as global AOD decreases and the influence of GHGs  
280 strengthen. However, AERs remain the dominant contributor to forced historical (ALL)  
281 precipitation trends over densely populated regions in the summer months of each hemisphere  
282 (Figure 1h, 1i), demonstrating that AERs drive human exposure to precipitation change  
283 throughout the historical period.

284  
285 In the mid-20th century (1930 to 1979), the absolute effect of AERs is greater than the  
286 absolute effect of GHGs and any other residual natural and/or anthropogenic forcings over  
287 almost all land regions (Figure 2a-2c). In the annual-mean, AERs overwhelm opposing GHG  
288 signals over most regions (red shading). However, in some key areas (particularly in the  
289 subtropical and semiarid regions of Central America, Africa, and Australia), AERs dominate a  
290 complementary GHG signal (green shading). Summertime precipitation trends show AER  
291 dominance over more regions in both hemispheres compared with the annual-mean, but AER  
292 and GHG effects tend to be reinforcing rather than opposing (Figure 2b, 2c).

293  
294 In the late 20th century (1950 to 1999), AER dominance reduces, following the peak and  
295 decline of AOD in North America and Europe and the redistribution of AOD to the Eastern  
296 Hemisphere (Figure 1b). However, in the annual-mean, AERs still overwhelm opposing GHG  
297 signals over highly populated regions (Figure 2d). In Northern and Western Australia, West  
298 Africa, and the Middle East, with notably small in situ AER loading (Figure 1b), AERs dominate  
299 a complementary GHG signal (Figure 2d), evidence of teleconnected effects (71, 72). Annual-  
300 mean AER dominance can be consistent across seasons (South and East Asia, Figure 2d, 2e, 2f),  
301 driven by a strong response in a particular season (Australia in DJF, Figure 2f), or can occur  
302 mainly in a specific season with opposing sign as the annual-mean (Eastern North America and  
303 Sahara, Figure 2e), demonstrating the numerous ways in which AERs control local and seasonal  
304 precipitation.

305  
306 At the turn of the 21st century (1970 to 2019), anthropogenic AOD declines globally and  
307 relocates hemispherically (73), resulting in a diminished role for AERs overall. Regardless, AER  
308 dominance is maintained within highly populated regions in summer (Figure 2h, 2i). Seasonal  
309 AER dominance is more confined to highly populous areas during this period compared to either  
310 late 20th-century interval (Figure 2e, 2f). This manifests as annual-mean dominance in only a  
311 handful of regions (Figure 2g). This demonstrates the importance of seasonal attribution, as  
312 climatological precipitation and AER forcing both have notable seasonal variations.

313  
314 **Regional decomposition of aerosol-dominated precipitation trends throughout the 20th**  
315 **and early 21st century.** The variable pathways through which AERs control historical  
316 precipitation arise from thermodynamic and dynamic influences on local and/or large-scale  
317 circulation patterns, resulting in regionally specific impacts (Figure 1). The regional precipitation  
318 response to GHGs can further conflate this influence, as the effects of the two anthropogenic  
319 forcings on precipitation can either reinforce or counteract each other in the total precipitation  
320 response (Figure 2). Hence, assessing the mechanisms through which AERs dominate regional

321 historical precipitation trends in the presence of GHGs and other forcings requires spatially  
322 resolved analysis within the region of interest. We explore this aspect by highlighting the ALL,  
323 AER, GHG, and AER+GHG precipitation trends across the three trend periods in two highly  
324 populated regions, North America and Asia (Figure 3), which have diverse precipitation  
325 climatologies and therefore differing pathways of AER influence in JJA. Other regions, seasons,  
326 and individual model results are provided in Supplementary Figures S2-S104.

327  
328 Spatially resolved analysis of North American (NAM) precipitation trends reveals that AERs  
329 dominate forced historical precipitation trends despite a highly variable spatial and temporal  
330 evolution alongside monotonically increasing GHG forcing. In the early period, AERs dominate  
331 forced (ALL) precipitation trends across NAM (Figure 2b). Rising AOD over the Eastern United  
332 States (Figure 1a; (2) drives localized drying, large-scale Canadian drying, and wetting over the  
333 Central United States (Figure 3b). This pattern can also be seen in ALL (Figure 3a). However,  
334 the magnitude of AER-driven Canadian drying is partially offset by GHG-driven wetting (Figure  
335 3c). In the middle period, the forced precipitation signal is indistinguishable from internal  
336 variability over the continental United States; only one model shows a significant trend in ALL,  
337 AER, or GHG (Figure S9). Although AER-driven wetting in the Western and Central United  
338 States and drying in the Eastern United States is the strongest anthropogenic signal in the middle  
339 period (Figure 2e, Figure 3f-h), the signal is sufficiently weak that it is overwhelmed by internal  
340 variability and nonlinearities when combined with weaker but opposing GHG-driven effects in  
341 the historical forced signal (Figure 3e). Over Canada, weaker AER-driven drying is  
342 overwhelmed by strengthened GHG-driven wetting, resulting in regional wetting in the forced  
343 historical response (Figure 3e, 3f, 3g). In the late period, the forced precipitation response is  
344 dominated by GHG-driven wetting across Canada, but by AER-driven effects across the  
345 continental United States. Remotely, AER-driven drying accounts for forced historical drying  
346 trends across the agriculturally-active Western United States and Great Plains regions (Figure 2h,  
347 3i, 3j, 3k), while decreasing AOD over the heavily populated Eastern United States (Figure 1c;  
348 (2) drives localized wetting, which compounds with the spatially homogenous GHG-driven  
349 wetting to produce the total forced response.

350  
351 Spatially resolved analysis of Asian precipitation trends shows that AER dominance arises  
352 through combined remote and local effects (23), which are not distinguishable in spatial-mean  
353 metrics, but have different temporal and sub-regional behavior. In the early period, AERs  
354 dominate forced precipitation trends over Asia (Figure 2b). Increases in North American and  
355 European AOD during this period (Figure 1a) weakened the South and East Asian monsoons  
356 (21, 23, 26), reducing precipitation across the entire continent in both AER and ALL (Figure 3n,  
357 3o). In the middle period, AERs still dominate the forced historical South and East Asian drying  
358 (Figure 1e), although model dependency obscures the Asian AER response (Figure S68). Local  
359 Asian AOD rises as remote emissions begin their decline (Figure 1b), leading to an even larger  
360 AER-driven drying in South and East Asia, with greater influence from local emissions than in  
361 the early period (Figure 3s; (23). However, in the late period, a dipole emerges in the forced  
362 responses through a complex interaction amongst local AER-, remote AER-, and GHG-driven  
363 effects. AERs still dominate South and East Asian forced precipitation trends (Figure 1h).  
364 However, drying over Southern China in AER and ALL (Figure 3v, 3w) arises from increased  
365 local AOD and associated weakening of the East Asian monsoon (46). Meanwhile, the forced

366 late period wetting in South Asia and northern China arises from the convergence of intensifying  
367 GHG-driven wetting and the reversal of remote AER-driven drying as NH extratropical AOD  
368 trends become negative (23). However, despite the increased influence of GHG-driven wetting in  
369 the late period (Figure 3x), AERs still dominate the damping of the South and East Asian  
370 monsoons over the populated regions (Figure 2h).

371  
372 The spatially-resolved perspective reveals the complexities in how changes in AERs  
373 dominate historical precipitation trends, which may be overlooked in regional-mean metrics. The  
374 spatiotemporally nonuniform changes in AER-driven precipitation illustrate the shortcomings of  
375 attempting to scale AER-driven hydroclimate impacts with common proxies such as local or  
376 global AOD, emissions, or radiative forcing, as is often done with GHG forcing, when estimating  
377 the regional precipitation responses to AERs through time (74–76). Given pervasive AER  
378 dominance of regional precipitation trends (Figure 2), this also demonstrates the importance of  
379 carefully evaluating AERs’ role in regional precipitation signals.

380  
381 **Limitations of common scaling approaches for estimating aerosol-driven precipitation**  
382 **change.** Constraining the distinct and regionally variable dominance of AERs on historical  
383 precipitation is key to detection and attribution and to evaluating future climate projections and  
384 associated climate risk. Yet, AERs’ impact on historical precipitation is often underrepresented or  
385 treated as a scalable offset to GHG-driven change (30, 77–79). The mechanistic differences of  
386 AERs from the response to GHGs demonstrate that AERs’ precipitation impacts must be  
387 considered independently and often will not scale well with proxies commonly used to produce  
388 simplified projections of GHG-driven impacts. To illustrate these points quantitatively, we now  
389 present an assessment of the validity of certain common scaling approaches through a  
390 comparison of global annual-mean near-surface air temperature change (Figure 4c), global  
391 annual-mean apparent hydrological sensitivity (Figure 4d), and the resulting precipitation change  
392 from the pre-industrial at a given Global Warming Level (GWL) in a GHG (Figure 4a), ALL  
393 (Figure 4b), and AER (Figure 4e) forcing scenario.

394  
395 In the multi-model mean and across individual LESFMIP models, AERs produce a higher  
396 apparent hydrological sensitivity than GHGs (Figure 4d), calculated as the total percentage  
397 change in global precipitation since pre-industrial times per degree of global-mean temperature  
398 change (67, 80). While GHGs more strongly contribute to forced historical (ALL) temperature  
399 changes (Figure 4c), AERs have a larger impact on forced historical precipitation changes per  
400 degree of global temperature change. Hence, the historical all-forced apparent hydrological  
401 sensitivity is greatly influenced by AER-driven precipitation change (Figure S108) and is  
402 therefore time-varying and negative across almost all models in the late 20th century (1950 to  
403 1990), when AER emissions evolved rapidly globally (Figure 4d). This considerable influence of  
404 AERs further supports that real-world hydrological sensitivity is likely susceptible to the  
405 combination of future AER and GHG forcing (61), which is highly uncertain (13, 81). Therefore,  
406 there is no single historical-mean hydrological sensitivity that can be used for future projections  
407 without understanding the future evolution of the AER forcing.

408

409 These results further demonstrate that GWL (82) and pattern scaling (76, 83, 84) approaches  
410 are likely to misrepresent hydroclimate signals when AERs play a considerable role in the total  
411 forced response. Figure 4c highlights the differing precipitation patterns that emerge at a GWL of  
412 +0.5K when that threshold is achieved though all anthropogenic forcings versus only GHGs. The  
413 GHG-driven change in temperature reaches +0.5 K GWL in 1960, while the all-forced change in  
414 temperature does not reach this threshold until 1987 due to the counteracting AER-driven  
415 cooling. The precipitation changes at the same GWL differ not only in spatial pattern but also in  
416 global-mean sign. At a GWL of +0.5 K, GHGs drive a global-mean change in precipitation of  
417 0.023 mm/day, with notable increases in precipitation over the tropical rain belt, mild drying  
418 across the subtropics, and wetting at higher latitudes (Figure 4a). In contrast, at the same GWL,  
419 historical anthropogenic forcings produce a global-mean change in precipitation of -0.006  
420 mm/day and drive a southward shift of the ITCZ, as well as large-scale drying over Southeast  
421 Asia, Southern Africa, and Northern South America (Figure 4b). The corresponding AER-driven  
422 change in precipitation centered around 1987 has a global-mean value of -0.055 mm/day with a  
423 pronounced southward shift of the ITCZ in all three ocean basins, marked drying over South  
424 Asia, and milder drying (wetting) at high (subtropical) latitudes (Figure 4e). These results  
425 emphasize that although GHGs drive more of the forced historical temperature change than  
426 AERs (Figure 4c), the high apparent hydrological sensitivity of AERs (Figure 4d) results in a  
427 larger influence of AERs on forced historical precipitation change than GHGs at a given GWL.  
428 This affirms that the historical precipitation response to warming is a strong function of the  
429 combination of AER and GHG forcing. Furthermore, using a historical-mean value to extrapolate  
430 the sensitivity of global-mean precipitation change to future warming, as is pursued in GWL or  
431 pattern scaling approaches, will be problematic as the mix of AERs and GHGs rapidly evolve  
432 (76, 85).

433  
434

### 435 III. Summary and Implications

436

437 In this study, we utilize five Large Ensemble Single Forcing Model Intercomparison Project  
438 (LESFMIIP) models (CanESM5, CESM2, CNRM-CM6-1, IPSL-CM6-LR, MIROC6) with  
439 historical all-forcing (ALL), anthropogenic aerosol-only (AER), and greenhouse gas-only (GHG)  
440 simulations ranging from 9 to 65 ensemble members each. We identify the temporal and regional  
441 dominance that anthropogenic aerosols have had on forced historical precipitation trends, and  
442 their co-evolution with greenhouse gas-driven effects. We find that anthropogenic aerosols  
443 dominate forced historical precipitation trends in densely populated regions, sometimes  
444 reinforcing and sometimes offsetting greenhouse gas-driven impacts. Anthropogenic aerosols'  
445 influences on precipitation derive from both local and remote emissions via a mix of radiative  
446 and dynamical pathways, whose relative importance depends on the region and season of  
447 interest.

448

449 The results presented here highlight that current approaches that overlook the unique  
450 contribution of anthropogenic aerosols to hydroclimate change are likely to oversimplify the  
451 historical impacts of anthropogenic aerosols and misrepresent the future influence of

452 anthropogenic emissions on the climate system and society. We show that anthropogenic  
453 aerosols' influence on regional precipitation is outsized relative to its impact on global-mean  
454 temperature and does not scale with proxies like global (or even local) AOD, emissions, or  
455 radiative forcing. Thus, the many detection and attribution techniques that use these proxies to  
456 establish time-evolving fingerprints for different forcings' role in historical precipitation signals  
457 (74, 75) are likely misrepresentative. Extreme event attribution protocols, meanwhile, do not  
458 differentiate the contribution of aerosols versus greenhouse gases to an identified anthropogenic  
459 contribution or may exclude the aerosol signal altogether (77–79), which our results suggest is  
460 problematic for precipitation-related extreme events, given aerosols' dominance over most  
461 populated regions. This historical dominance also highlights that future changes in anthropogenic  
462 aerosol emissions are likely to be a substantial contributor to future precipitation trends,  
463 associated climate risk, and socio-economic impacts. Hence, constraining the uncertainty in  
464 future aerosol emissions and the composite effects with greenhouse gas emissions (e.g., through  
465 the Regional Aerosol Model Intercomparison Project; (81) will be essential for identifying future  
466 precipitation controls.

467  
468 Our results are based on the most comprehensive dataset to date for addressing  
469 anthropogenic aerosols' role in forced precipitation change, overcoming limitations associated  
470 with uncertainty due to internal variability and models' structural differences. As such, our study  
471 presents a robust quantification of anthropogenic aerosols' unique and evolving influence on past  
472 hydrologic change, with implications for planning and adaptation to future hydroclimate risks.  
473 However, the inherent complexity of anthropogenic aerosol-driven signals that we demonstrate  
474 here highlights the need for continuing mechanistic analysis to understand and quantify the  
475 processes underlying the evolving influence of anthropogenic aerosols on historical precipitation  
476 at regional and global scales. Dynamical decomposition of the driving mechanisms behind these  
477 precipitation responses to anthropogenic aerosols across LESFMIP models is not included in this  
478 study and will be valuable to definitively understand how shifting emissions patterns affect  
479 precipitation responses, in combination with the many prior studies based on single models,  
480 smaller ensemble sizes, and older CMIP versions.

481  
482 The spatiotemporal complexity of the anthropogenic aerosol-driven signal presented here has  
483 important implications for how anthropogenic forcing is characterized across a range of scientific  
484 and decision-making applications. Spatial-mean estimates of forced precipitation change (e.g.,  
485 Figure 1, Figure 2) could misrepresent the geographically diverse effect of forcings on  
486 precipitation when used in isolation. Geographic cancellation of both positive and negative  
487 trends is present in anthropogenic aerosol-forced (and to a lesser extent greenhouse gas-forced)  
488 precipitation change (e.g., East Asian historical precipitation response in the late period; Figure  
489 1k, 3v), which could significantly weaken the detected forced response in regional-mean metrics  
490 even when anthropogenic influence is large and can lead to conflicting conclusions about the role  
491 of anthropogenic aerosols in a given region. Hence, methodology should be chosen carefully so  
492 as not to oversimplify the anthropogenic aerosol variability in space, time, or magnitude.  
493

494 Interpreting and improving model representation of the anthropogenic aerosol signal is a  
495 persistent and growing priority in the climate science community (4, 86–88), but should account  
496 for the fact that not all forms of model disagreement on the anthropogenic aerosol signal are  
497 created equal. Despite the identical CMIP6 anthropogenic aerosol emissions used in each  
498 LESFMIP model, structural differences across models (e.g., due to representation of sub-grid  
499 processes and parameterizations, feedback mechanisms, aerosol-cloud interactions, ocean-  
500 atmosphere coupling, and resolution, among others; (88) result in a range of anthropogenic  
501 aerosol forcing and response. In the late-20th century (1950 to 1999), the geographic distribution  
502 of anthropogenic aerosol emissions shifted rapidly, and the models’ structural differences  
503 produce different timescales of response. This results in high model disagreement during the  
504 middle period due to the differing model adjustment times, even though the final late period  
505 response is similar (e.g., representation of African ITCZ shift across models, Figure S53-S55).  
506 On the other hand, model disagreement in the anthropogenic aerosol-forced response also arises  
507 from biases in precipitation climatology (e.g., representation of Asian monsoon climatology  
508 across models, Figure S67-S69) which does not resolve as the models adjust to changing  
509 anthropogenic aerosols. These two sources of disagreement have different solution strategies and  
510 different implications for constraining uncertainty in the historical role of anthropogenic aerosols  
511 and projected impacts on precipitation.

512  
513 Finally, our results highlight that regional precipitation responses to anthropogenic aerosols  
514 at a particular point in time can be highly dependent on the local climatological drivers of  
515 precipitation and the global distribution (not just amount) of emissions. Consequently, identical  
516 anthropogenic aerosol emissions cannot be expected to affect precipitation in the same way in  
517 each region (44). Therefore, the same analytical framework (e.g., scaling techniques) cannot be  
518 applied globally or uniformly through time in the way some emissions-driven emulators (6),  
519 regional climate models (89), or pattern scaling approaches (90) do (Figure 4). Given the  
520 potential magnitude of resulting hazards and socio-economic impacts (91), targeted assessment  
521 of the role of anthropogenic aerosol forcing in regional hydroclimate change should be  
522 prioritized.

#### 523 524 525 **IV. Materials and Methods**

526  
527 Here, we use five of the 6th Coupled Model Intercomparison Project (CMIP6) models  
528 following the Large Ensemble Single Forcing Model Intercomparison Project (LESFMIP; (62)  
529 protocol, with forcings defined by CMIP6 (92). These include historical all-forcing (ALL),  
530 anthropogenic aerosol-only (AER), and well-mixed greenhouse gas-only (GHG) simulations,  
531 post-processed by the Climate Variability and Diagnostics Package version 6 (CVDPv6; (93) for  
532 three 50-year trend periods. We discuss the models, simulation post-processing, and analysis  
533 methodology further below.

##### 534 535 ***A. Large Ensemble Single Forcing Model Intercomparison Project (LESFMIP) Protocol***

536

537 Observations alone make it difficult to separate external influences on climate from the  
538 internal variability of the natural system (94). Hence, large ensembles of simulations from one  
539 model with the same forcing, but varied initial conditions, allow for the detection of a forced  
540 signal in the ensemble-mean amongst the natural noise of the modeled system (2, 9, 59, 94).  
541 Larger ensemble suites allow for more robust signal detection, but can be computationally  
542 expensive. Anywhere from five to 100 ensemble members could be required, depending on the  
543 climate variable, application, location, geographic scale, and time frame of results (59, 94, 95).  
544 The Large Ensemble Single Forcing Model Intercomparison Project (LESFMIP; (62) aims to  
545 directly address this issue across models by including historical simulations identical to those  
546 proposed by the Detection and Attribution Model Intercomparison Project (DAMIP; (96) and  
547 climate forcings defined by CMIP6 (92), but with 10-50 ensemble members requested from  
548 participating models (62).

549  
550 In this study, we utilize historical (ALL, all forcings), hist-aer (AER, anthropogenic-aerosol-  
551 only historical simulations), and hist-GHG (GHG, well-mixed greenhouse-gas-only simulations)  
552 LESFMIP simulation output (62) from five participating CMIP6 models: version 5 of the  
553 Canadian Earth System Model (CanEMS5; (97), version 2 of the Community Earth System  
554 Model (CESM2; (98), version 6 of the Centre National de Recherches Météorologiques and  
555 Cerfacs coupled model (CNRM-CM6-1; (99), version 6 of the Institut Pierre-Simon Laplace  
556 coupled model (IPSL-CM6A-LR; (100), and version 6 of the Model for Interdisciplinary  
557 Research on Climate (MIROC6; (101). Additionally, we include linearly added ensemble-mean  
558 AER+GHG results to highlight the role of nonlinearities or other natural and/or anthropogenic  
559 forcings not included in this study. Ensemble member amounts for each LESFMIP model and  
560 simulation are listed in Table S1. A detailed description of components, aerosol effective  
561 radiative forcing (ERF), aerosol representation, and climate sensitivities for participating  
562 LESFMIP models is listed in Table S2.

### 563 564 ***B. Climate Variability and Diagnostics Package version 6 (CVDPv6) Post Processing***

565  
566 Most LESFMIP simulation output in this study has been post-processed using the Climate  
567 Variability Diagnostics Package version 6 (CVDPv6), developed by the Climate Analysis Section  
568 (CAS) at the National Center for Atmospheric Research (NCAR). The CVDPv6 is an automated  
569 analysis tool and data repository that assesses modes of climate variability and trends in  
570 individual models, large ensemble suites, and observations, and provides quantitative  
571 comparisons across each (93).

572  
573 Three overlapping 50-year trend periods (1930 to 1979, 1950 to 1999, and 1970 to 2019)  
574 were chosen for the CVDPv6 output, following Deser et al. 2020 (2). It is important to note that  
575 historical (ALL) simulations only span to 2014, while hist-aer and hist-GHG span to 2019 using  
576 SSP2-4.5 emissions, following the DAMIP protocol (SSP3-7.0 for CESM2, following CESM2  
577 Single Forcing Large Ensemble Project; (102). 50-year trends (+/- 10 years) were found to  
578 effectively accommodate the temporal and spatial evolution of the anthropogenic aerosol and  
579 well-mixed greenhouse gas forcing and response. These three trend periods capture the slow  
580 changes in aerosol optical depth (AOD) globally and highlight significant shifts in the  
581 geographical location of AOD, including: The rise in North American and European AOD from  
582 1930 to 1979, the tropical geographical shift towards South America and Africa from 1950 to

583 1999, and the continual rise of South Asian AOD as North American and European AOD  
584 decreases from 1970 to 2019 (2). Notably, there are regional changes in AOD within these 50-  
585 year periods (e.g., the rise and fall of AOD in China from 2000 to the present; (73), but we aim to  
586 capture the global-scale shifts in AOD. These trend periods are referred to as the “early”,  
587 “middle”, and “late” time periods in the text, respectively. Noteworthy global results have been  
588 confirmed with two non-overlapping 40-year trend periods of 1940 to 1979 and 1980 to 2019,  
589 motivated by the possibility that the peak and fall of North American and European AOD that  
590 both occur in middle period could result in an underestimation of absolute AER effects. These  
591 non-overlapping periods yield little change in statistically significant results (not included).  
592 However, variable signals would likely arise in regional results, depending on the period chosen  
593 and the specific geographical location. A detailed analysis of different trend intervals could  
594 highlight how regional precipitation responses vary based on the period chosen and the given  
595 anthropogenic aerosol emission distribution.

596

### 597 *C. Observational Dataset and Comparison*

598

599 We utilize the Global Precipitation Climatology Center (GPCC) v. 2022 observations, post-  
600 processed by the CVDPv6, from corresponding 50-year trend periods as modeled results.  
601 GPCCv2022 provides land-surface station gauge data at the 1.0-degree resolution from 1891 to  
602 2022 (103). However, gauge station sites are variable and could be sparse or inhomogeneous  
603 across grid cells, leading to spurious temporal variability in precipitation data. General  
604 circulation models have also been shown to underestimate precipitation compared to  
605 observations due to their coarse resolution and inability to resolve small-scale cloud and rainfall  
606 processes, which is a persistent issue in CMIP6 models. Observational comparison with modeled  
607 LESFMIP results is included in the supplementary material (Figure S105-S107). Results show  
608 that while all five models underestimate precipitation compared to GPCC due to ensemble-mean  
609 signal damping, GPCC observations fall within the spread of ensemble members of at least one  
610 of the LESFMIP models in almost all regions (Figure S105). Hence, the observed climate  
611 trajectory is likely captured in the LESFMIP ensemble spread, with specific models performing  
612 better in certain regions, despite underestimation in the ensemble-mean signals.

613

### 614 *D. Analysis Methods*

615

616 All models’ linear trends are computed using a linear regression during CVDPv6 post-  
617 processing. A Student’s two-sided one-sample T-test is used to calculate significance at the 95%  
618 confidence interval (45) for a model’s ensemble-mean trends (e.g., Figure S4). Individual  
619 ensemble member trend values populate T-tests for ALL, AER, and GHG simulations. For  
620 AER+GHG, unique pairs are made across individual AER and GHG ensemble members up to  
621 the maximum ensemble member size between AER and GHG, which populate a distribution for  
622 the Student’s T-test. Some individual ensemble members are repeated in pairs, but since they are  
623 paired with a new and unused corresponding ensemble member, we consider this a unique pair.  
624 When applied to a model’s trends across ensemble members, this Student’s one-sample T-test  
625 captures whether the forced trend value at that grid point is statistically significantly different  
626 than zero, given the spread of internal variability.

627

628 In multi-model mean regional plots (e.g., Figure 3), significance is shown where four out of  
629 five models agree on sign, following the Intergovernmental Panel on Climate Change  
630 Assessment Report 6 (IPCCAR6) methodology (104).

631  
632 For spatial-mean trend values (e.g., Figure 1e-k), a Wald Test is performed on transient  
633 LESFMIP simulations to obtain the standard error from the linear regression. This Wald test  
634 captures whether the forced (ensemble-mean) trend is statistically distinguishable from zero,  
635 given the year-to-year variability of the forced signal through time. The standard error represents  
636 the temporal robustness of the forced signal, with small standard errors indicating a more  
637 consistent and reliable forced trend over time. The mean of the individual model's standard  
638 errors is used in model-mean results.

639  
640 All models' native grid spacing is preserved for individual modeled plots (e.g., Figure S4)  
641 from the CVDPv6 and is linearly interpolated to the lowest resolution (CanESM5) for multi-  
642 model means (e.g., Figure 3). However, the transient simulations used in the Wald Test for trend  
643 standard error are all regridded to the CESM1 grid spacing (192 lat x 288 lon) using a bilinear  
644 interpolation prior to significance calculations, leading to a negligibly high-biased standard error  
645 from the Wald Test.

646  
647 Area weighting is performed on all regional-mean, global-mean, and time series results, as  
648 well as in Pearson's correlation coefficient calculations (pattern correlations, Figure 3) after the  
649 spatial-mean has been removed.

650  
651 An absolute trend calculation is used to determine anthropogenic aerosol dominance of  
652 forced historical precipitation trends (e.g., Figure 2). In each individual IPCC region highlighted,  
653 we obtain the absolute value of the (ensemble- and model-mean) ALL, AER, GHG, and  
654 AER+GHG CVDPv6 precipitation trends in that region. We then calculate the area-weighted  
655 spatial-mean of the absolute values. If the absolute AER spatial-mean in a given region is greater  
656 than both the absolute GHG and absolute residual (ALL – AER+GHG), then we consider AERs  
657 to dominate ALL precipitation trends in that region. Stippling shows land masked population  
658 density > 100 ppl/km<sup>2</sup> in the later trend period based on Socioeconomic Data and Applications  
659 Center (SEDAC) Global Population of the World Version 4, revision 11 (GPWv4.11) 2020 (105).

660  
661 We calculate apparent hydrological sensitivity (AHS) as the total percentage change in  
662 global-mean precipitation divided by the change in global-mean near-surface air temperature  
663 relative to a pre-industrial mean (1850-1880) in ALL, AER, and GHG ( $AHS = \Delta P_{glob} / \Delta T_{glob}$ ,  
664 following the methodology of (80)).

665  
666  
667  
668

### Acknowledgements

669 This work is partially supported by the National Science Foundation's Climate and  
670 Large-Scale Dynamics program under award #2235177 (KW, GGP, CD, ASP, XZ) and the  
671 Heterogeneous Climate Forcing (HETCLIF) project under the Center for Advanced Study at the  
672 Norwegian Academy of Science and Letters' Research Grant (KW, GGP, BHS, LJW, MTL).  
673 Authors are further supported by the University of Texas at Austin Department of Earth and

674 Planetary Sciences (KW, GGP, XZ), National Center for Atmospheric Research (NCAR; CD,  
675 ASP, XZ), CICERO Center for International Climate Research (BHS, MTL), Research Council  
676 of Norway grant no. 324182 (CATHY; BHS, LJW, MTL), National Centre for Atmospheric  
677 Science (NCAS; LJW), Horizon Europe grant 101137639 (CleanCloud; BHS, MTL, LJW), and  
678 the Natural Environment Research Council (NERC; grant NE/W004895/1, TerraFIRMA; LJW).  
679 We would like to acknowledge computing support from the Cheyenne  
680 (doi:10.5065/D6RX99HX) and Casper systems provided by the National Science Foundation  
681 (NSF) NCAR, sponsored by the NSF. We would like to thank participating Regional Aerosol  
682 Model Intercomparison Project (RAMIP) collaborators for their helpful conversation, developers  
683 of the Climate Variability Diagnostics Package version 6 (CVDPv6) for the LESFMIP data  
684 assimilation, and Cameron Cummins for assistance with making the figure scripts and datasets  
685 publicly accessible.

### 686 687 **Data Availability** 688

689 Model output from LESFMIP is publicly available through the Earth System Grid  
690 Federation (ESGF), but the CVDPv6 postprocessed and transient LESFMIP data used here is  
691 available for download through a Globus Guest Collection at ([https://app.globus.org/file-  
692 manager?origin\\_id=21b869ac-7c56-4dd7-bfa8-89ebc3cda4c1&origin\\_path=%2F](https://app.globus.org/file-manager?origin_id=21b869ac-7c56-4dd7-bfa8-89ebc3cda4c1&origin_path=%2F)). Community  
693 Emissions Data System (CEDS) for Historical Emissions v. 2017-05-18 annual anthropogenic  
694 SO<sub>2</sub> emissions dataset prepared for input4MIPs is available through ESGF. The Socioeconomic  
695 Data and Applications Center (SEDAC) Gridded Population of World, version 4 (GPWv4) 2020  
696 Population Density, Revision 11 can be found at ([https://earth.gov/ghgcenter/data-catalog/sedac-  
697 popdensity-yeargrid5yr-v4.11](https://earth.gov/ghgcenter/data-catalog/sedac-popdensity-yeargrid5yr-v4.11)).

### 698 699 **Code Availability** 700

701 All code and scripts used in this study are available for download through a GitHub  
702 repository at (*Link to private repository available to reviewers upon request. Will make public  
703 and paste link here upon acceptance of manuscript*).

### 704 705 706 **References** 707

- 708 1. O. Boucher, D. A. Randall, P. Artaxo, Chapter 7: Clouds and Aerosols. (2013).
- 709 2. C. Deser, *et al.*, Isolating the Evolving Contributions of Anthropogenic Aerosols and  
710 Greenhouse Gases: A New CESM1 Large Ensemble Community Resource. *J. Clim.* **33**,  
711 7835–7858 (2020).
- 712 3. G. Myhre, *et al.*, Chapter 8: Anthropogenic and Natural Radiative Forcing. (2013).
- 713 4. N. Bellouin, *et al.*, Bounding Global Aerosol Radiative Forcing of Climate Change. *Rev.*  
714 *Geophys.* **58**, e2019RG000660 (2020).

- 715 5. P. Forster, T. Storelvmo, K. C. Armour, Chapter 7: The Earth's Energy Budget, Climate  
716 Feedbacks, and Climate Sensitivity. *The Earth* 132 (2021).
- 717 6. S. Szopa, V. Naik, B. Adhikary, Chapter 6: Short-Lived Climate Forcers. 106 (2021).
- 718 7. C. Diao, Y. Xu, S.-P. Xie, Anthropogenic aerosol effects on tropospheric circulation and  
719 sea surface temperature (1980–2020): separating the role of zonally asymmetric forcings.  
720 *Atmospheric Chem. Phys.* **21**, 18499–18518 (2021).
- 721 8. Y. Dong, J. E. Kay, C. Deser, A. Capotondi, S. C. Sanchez, Distilling the Evolving  
722 Contributions of Anthropogenic Aerosols and Greenhouse Gases to Large-Scale Low-  
723 Frequency Surface Ocean Changes Over the Past Century. *Geophys. Res. Lett.* **51**,  
724 e2024GL112020 (2024).
- 725 9. J.-R. Shi, Y.-O. Kwon, S. E. Wijffels, Two Distinct Modes of Climate Responses to the  
726 Anthropogenic Aerosol Forcing Changes. *J. Clim.* **35**, 3445–3457 (2022).
- 727 10. D. T. Shindell, G. Faluvegi, L. Rotstayn, G. Milly, Spatial patterns of radiative forcing and  
728 surface temperature response. *J. Geophys. Res. Atmospheres* **120**, 5385–5403 (2015).
- 729 11. B. H. Samset, M. T. Lund, M. Bollasina, G. Myhre, L. Wilcox, Emerging Asian aerosol  
730 patterns. *Nat. Geosci.* **12**, 582–584 (2019).
- 731 12. X. Zhao, *et al.*, Separating radiative and SST-induced impacts of time-evolving industrial  
732 and biomass burning aerosols on historical boreal summer climate. Unpublished  
733 manuscript. Submitted to *J. Clim.*
- 734 13. M. T. Lund, G. Myhre, B. H. Samset, Anthropogenic aerosol forcing under the Shared  
735 Socioeconomic Pathways. *Atmospheric Chem. Phys.* **19**, 13827–13839 (2019).
- 736 14. C. J. W. Bonfils, *et al.*, Human influence on joint changes in temperature, rainfall and  
737 continental aridity. *Nat. Clim. Change* **10**, 726–731 (2020).
- 738 15. Y.-T. Hwang, D. M. W. Frierson, S. M. Kang, Anthropogenic sulfate aerosol and the  
739 southward shift of tropical precipitation in the late 20th century. *Geophys. Res. Lett.* **40**,  
740 2845–2850 (2013).
- 741 16. Y. Ming, V. Ramaswamy, A Model Investigation of Aerosol-Induced Changes in Tropical  
742 Circulation. (2011). <https://doi.org/10.1175/2011JCLI4108.1>.
- 743 17. R. J. Allen, A. T. Evan, B. B. Booth, Interhemispheric Aerosol Radiative Forcing and  
744 Tropical Precipitation Shifts during the Late Twentieth Century. (2015).  
745 <https://doi.org/10.1175/JCLI-D-15-0148.1>.
- 746 18. K. Marvel, M. Biasutti, C. Bonfils, Fingerprints of external forcings on Sahel rainfall:  
747 aerosols, greenhouse gases, and model-observation discrepancies. *Environ. Res. Lett.* **15**,  
748 084023 (2020).

- 749 19. P.-A. Monerie, A. J. Dittus, L. J. Wilcox, A. G. Turner, Uncertainty in Simulating  
750 Twentieth Century West African Precipitation Trends: The Role of Anthropogenic Aerosol  
751 Emissions. *Earths Future* **11**, e2022EF002995 (2023).
- 752 20. B. Dong, R. T. Sutton, E. Highwood, L. Wilcox, The Impacts of European and Asian  
753 Anthropogenic Sulfur Dioxide Emissions on Sahel Rainfall. (2014).  
754 <https://doi.org/10.1175/JCLI-D-13-00769.1>.
- 755 21. M. A. Bollasina, Y. Ming, V. Ramaswamy, Anthropogenic Aerosols and the Weakening of  
756 the South Asian Summer Monsoon. *Science* **334**, 502–505 (2011).
- 757 22. P.-A. Monerie, L. J. Wilcox, A. G. Turner, Effects of Anthropogenic Aerosol and  
758 Greenhouse Gas Emissions on Northern Hemisphere Monsoon Precipitation: Mechanisms  
759 and Uncertainty. *J. Clim.* **35**, 2305–2326 (2022).
- 760 23. S. Undorf, *et al.*, Detectable Impact of Local and Remote Anthropogenic Aerosols on the  
761 20th Century Changes of West African and South Asian Monsoon Precipitation. *J.*  
762 *Geophys. Res. Atmospheres* **123**, 4871–4889 (2018).
- 763 24. G. G. Persad, Y. Ming, Z. Shen, V. Ramaswamy, Spatially similar surface energy flux  
764 perturbations due to greenhouse gases and aerosols. *Nat. Commun.* **9**, 3247 (2018).
- 765 25. S.-P. Xie, B. Lu, B. Xiang, Similar spatial patterns of climate responses to aerosol and  
766 greenhouse gas changes. *Nat. Geosci.* **6**, 828–832 (2013).
- 767 26. F. Song, T. Zhou, Y. Qian, Responses of East Asian summer monsoon to natural and  
768 anthropogenic forcings in the 17 latest CMIP5 models. *Geophys. Res. Lett.* **41**, 596–603  
769 (2014).
- 770 27. V. Hari, G. Villarini, S. Karmakar, L. J. Wilcox, M. Collins, Northward Propagation of the  
771 Intertropical Convergence Zone and Strengthening of Indian Summer Monsoon Rainfall.  
772 *Geophys. Res. Lett.* **47**, e2020GL089823 (2020).
- 773 28. S. M. Kang, S.-P. Xie, C. Deser, B. Xiang, Zonal mean and shift modes of historical  
774 climate response to evolving aerosol distribution. *Sci. Bull.* **66**, 2405–2411 (2021).
- 775 29. S. Fiedler, *et al.*, Anthropogenic aerosol forcing – insights from multiple estimates from  
776 aerosol-climate models with reduced complexity. *Atmospheric Chem. Phys.* **19**, 6821–6841  
777 (2019).
- 778 30. G. Persad, *et al.*, Rapidly evolving aerosol emissions are a dangerous omission from near-  
779 term climate risk assessments. *Environ. Res. Clim.* **2**, 032001 (2023).
- 780 31. M. Qin, A. Dai, W. Hua, Aerosol-forced multidecadal variations across all ocean basins in  
781 models and observations since 1920. *Sci. Adv.* **6**, eabb0425 (2020).
- 782 32. B. H. Samset, *et al.*, Fast and slow precipitation responses to individual climate forcers: A  
783 PDRMIP multimodel study. *Geophys. Res. Lett.* **43**, 2782–2791 (2016).

- 784 33. P. Stier, *et al.*, Multifaceted aerosol effects on precipitation. *Nat. Geosci.* **17**, 719–732  
785 (2024).
- 786 34. A. Voigt, *et al.*, Fast and slow shifts of the zonal-mean intertropical convergence zone in  
787 response to an idealized anthropogenic aerosol. *J. Adv. Model. Earth Syst.* **9**, 870–892  
788 (2017).
- 789 35. S. Zhang, P. Stier, D. Watson-Parris, On the contribution of fast and slow responses to  
790 precipitation changes caused by aerosol perturbations. *Atmospheric Chem. Phys.* **21**,  
791 10179–10197 (2021).
- 792 36. K. Carslaw, *Aerosols and Climate*, 1st Ed. (2022).
- 793 37. V. Ramanathan, P. J. Crutzen, J. T. Kiehl, D. Rosenfeld, Aerosols, Climate, and the  
794 Hydrological Cycle. *Science* **294**, 2119–2124 (2001).
- 795 38. T. Andrews, P. M. Forster, O. Boucher, N. Bellouin, A. Jones, Precipitation, radiative  
796 forcing and global temperature change. *Geophys. Res. Lett.* **37** (2010).
- 797 39. G. A. Ban-Weiss, L. Cao, G. Bala, K. Caldeira, Dependence of climate forcing and  
798 response on the altitude of black carbon aerosols. *Clim. Dyn.* **38**, 897–911 (2012).
- 799 40. D. Koch, A. D. Del Genio, Black carbon semi-direct effects on cloud cover: review and  
800 synthesis. *Atmospheric Chem. Phys.* **10**, 7685–7696 (2010).
- 801 41. G. G. Persad, D. J. Paynter, Y. Ming, V. Ramaswamy, Competing Atmospheric and  
802 Surface-Driven Impacts of Absorbing Aerosols on the East Asian Summertime Climate. *J.*  
803 *Clim.* **30**, 8929–8949 (2017).
- 804 42. T. Su, *et al.*, The significant impact of aerosol vertical structure on lower atmosphere  
805 stability and its critical role in aerosol–planetary boundary layer (PBL) interactions.  
806 *Atmospheric Chem. Phys.* **20**, 3713–3724 (2020).
- 807 43. A. Lewinschal, *et al.*, Local and remote temperature response of regional SO<sub>2</sub> emissions.  
808 *Atmospheric Chem. Phys.* **19**, 2385–2403 (2019).
- 809 44. G. G. Persad, The dependence of aerosols’ global and local precipitation impacts on the  
810 emitting region. *Atmospheric Chem. Phys.* **23**, 3435–3452 (2023).
- 811 45. G. G. Persad, K. Caldeira, Divergent global-scale temperature effects from identical  
812 aerosols emitted in different regions. *Nat. Commun.* **9**, 3289 (2018).
- 813 46. S. Undorf, M. A. Bollasina, G. C. Hegerl, Impacts of the 1900–74 Increase in  
814 Anthropogenic Aerosol Emissions from North America and Europe on Eurasian Summer  
815 Climate. (2018). <https://doi.org/10.1175/JCLI-D-17-0850.1>.
- 816 47. L. Liu, *et al.*, A PDRMIP Multimodel Study on the Impacts of Regional Aerosol Forcings  
817 on Global and Regional Precipitation. *J. Clim.* **31**, 4429–4447 (2018).

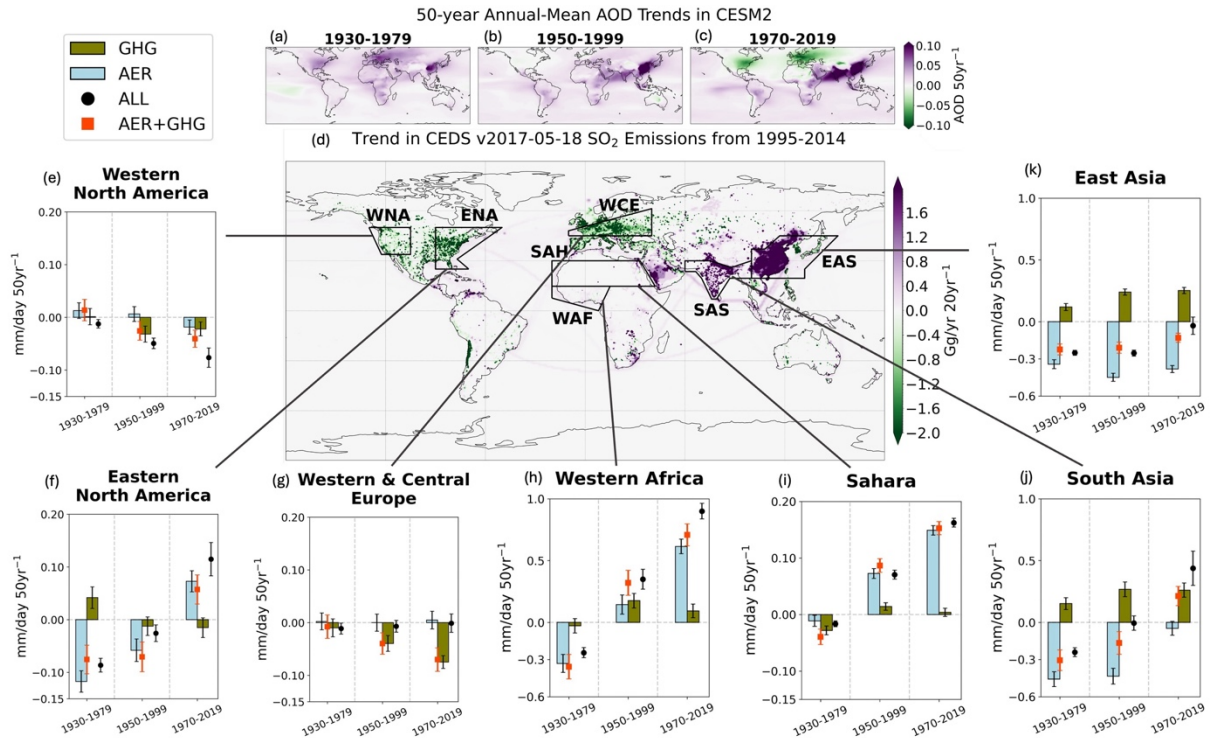
- 818 48. A. P. Schurer, A. P. Ballinger, A. R. Friedman, G. C. Hegerl, Human influence strengthens  
819 the contrast between tropical wet and dry regions. *Environ. Res. Lett.* **15**, 104026 (2020).
- 820 49. S.-P. Xie, *et al.*, Global Warming Pattern Formation: Sea Surface Temperature and  
821 Rainfall. (2010). <https://doi.org/10.1175/2009JCLI3329.1>.
- 822 50. B. B. B. Booth, N. J. Dunstone, P. R. Halloran, T. Andrews, N. Bellouin, Aerosols  
823 implicated as a prime driver of twentieth-century North Atlantic climate variability. *Nature*  
824 **484**, 228–232 (2012).
- 825 51. A. J. Dittus, E. Hawkins, J. I. Robson, D. M. Smith, L. J. Wilcox, Drivers of Recent North  
826 Pacific Decadal Variability: The Role of Aerosol Forcing. *Earths Future* **9**,  
827 e2021EF002249 (2021).
- 828 52. M. Qin, A. Dai, W. Hua, Quantifying Contributions of Internal Variability and External  
829 Forcing to Atlantic Multidecadal Variability Since 1870. *Geophys. Res. Lett.* **47**,  
830 e2020GL089504 (2020).
- 831 53. C. Xing, *et al.*, Apparent Changes in Pacific Decadal Variability Caused by  
832 Anthropogenically-Induced Mean State Modulations. [Preprint] (2024). Available at:  
833 [https://essopenarchive.org/users/855433/articles/1240284-apparent-changes-in-pacific-](https://essopenarchive.org/users/855433/articles/1240284-apparent-changes-in-pacific-decadal-variability-caused-by-anthropogenically-induced-mean-state-modulations?commit=2d4ba1faa050dc10af0fb364b1451dad4b6a3a6a)  
834 [decadal-variability-caused-by-anthropogenically-induced-mean-state-](https://essopenarchive.org/users/855433/articles/1240284-apparent-changes-in-pacific-decadal-variability-caused-by-anthropogenically-induced-mean-state-modulations?commit=2d4ba1faa050dc10af0fb364b1451dad4b6a3a6a)  
835 [modulations?commit=2d4ba1faa050dc10af0fb364b1451dad4b6a3a6a](https://essopenarchive.org/users/855433/articles/1240284-apparent-changes-in-pacific-decadal-variability-caused-by-anthropogenically-induced-mean-state-modulations?commit=2d4ba1faa050dc10af0fb364b1451dad4b6a3a6a) [Accessed 4  
836 September 2025].
- 837 54. M. B. Menary, *et al.*, Aerosol-Forced AMOC Changes in CMIP6 Historical Simulations.  
838 *Geophys. Res. Lett.* **47**, e2020GL088166 (2020).
- 839 55. D. Polson, M. Bollasina, G. C. Hegerl, L. J. Wilcox, Decreased monsoon precipitation in  
840 the Northern Hemisphere due to anthropogenic aerosols. *Geophys. Res. Lett.* **41**, 6023–6029  
841 (2014).
- 842 56. T. Tang, *et al.*, Dynamical response of Mediterranean precipitation to greenhouse gases and  
843 aerosols. *Atmospheric Chem. Phys.* **18**, 8439–8452 (2018).
- 844 57. L. Lin, Z. Wang, Y. Xu, Q. Fu, W. Dong, Larger Sensitivity of Precipitation Extremes to  
845 Aerosol Than Greenhouse Gas Forcing in CMIP5 Models. *J. Geophys. Res. Atmospheres*  
846 **123**, 8062–8073 (2018).
- 847 58. S. Pan, *et al.*, Larger Sensitivity of Arctic Precipitation Phase to Aerosol than Greenhouse  
848 Gas Forcing. *Geophys. Res. Lett.* **47**, e2020GL090452 (2020).
- 849 59. C. Deser, A. Phillips, V. Bourdette, H. Teng, Uncertainty in climate change projections: the  
850 role of internal variability. *Clim. Dyn.* **38**, 527–546 (2012).
- 851 60. G. Myhre, *et al.*, PDRMIP: A Precipitation Driver and Response Model Intercomparison  
852 Project—Protocol and Preliminary Results. *Bull. Am. Meteorol. Soc.* **98**, 1185–1198 (2017).

- 853 61. L. J. Wilcox, *et al.*, Accelerated increases in global and Asian summer monsoon  
854 precipitation from future aerosol reductions. *Atmospheric Chem. Phys.* **20**, 11955–11977  
855 (2020).
- 856 62. D. M. Smith, *et al.*, Attribution of multi-annual to decadal changes in the climate system:  
857 The Large Ensemble Single Forcing Model Intercomparison Project (LESFMIP). *Front.*  
858 *Clim.* **4** (2022).
- 859 63. R. M. Hoesly, *et al.*, Historical (1750–2014) anthropogenic emissions of reactive gases and  
860 aerosols from the Community Emissions Data System (CEDS). *Geosci. Model Dev.* **11**,  
861 369–408 (2018).
- 862 64. H. Hirasawa, P. J. Kushner, M. Sigmund, J. Fyfe, C. Deser, Anthropogenic Aerosols  
863 Dominate Forced Multidecadal Sahel Precipitation Change through Distinct Atmospheric  
864 and Oceanic Drivers. (2020). <https://doi.org/10.1175/JCLI-D-19-0829.1>.
- 865 65. H. Hirasawa, P. J. Kushner, M. Sigmund, J. Fyfe, C. Deser, Evolving Sahel Rainfall  
866 Response to Anthropogenic Aerosols Driven by Shifting Regional Oceanic and Emission  
867 Influences. (2022). <https://doi.org/10.1175/JCLI-D-21-0795.1>.
- 868 66. D. M. Westervelt, *et al.*, Connecting regional aerosol emissions reductions to local and  
869 remote precipitation responses. *Atmospheric Chem. Phys.* **18**, 12461–12475 (2018).
- 870 67. H. Douville, K. Raghavan, J. Renwick, Chapter 8: Water Cycle Changes. (2021).
- 871 68. B. H. Samset, Aerosol absorption has an underappreciated role in historical precipitation  
872 change. *Commun. Earth Environ.* **3**, 1–8 (2022).
- 873 69. L. Guo, A. G. Turner, E. J. Highwood, Local and Remote Impacts of Aerosol Species on  
874 Indian Summer Monsoon Rainfall in a GCM. (2016). <https://doi.org/10.1175/JCLI-D-15-0728.1>.
- 875
- 876 70. R. Herbert, L. J. Wilcox, M. Joshi, E. Highwood, D. Frame, Nonlinear response of Asian  
877 summer monsoon precipitation to emission reductions in South and East Asia. *Environ.*  
878 *Res. Lett.* **17**, 014005 (2022).
- 879 71. N. L. S. Fahrenbach, M. A. Bolasina, B. H. Samset, T. Cowan, A. M. L. Ekman, Asian  
880 Anthropogenic Aerosol Forcing Played a Key Role in the Multidecadal Increase in  
881 Australian Summer Monsoon Rainfall. (2024). <https://doi.org/10.1175/JCLI-D-23-0313.1>.
- 882 72. L. D. Rotstayn, *et al.*, Have Australian rainfall and cloudiness increased due to the remote  
883 effects of Asian anthropogenic aerosols? *J. Geophys. Res. Atmospheres* **112** (2007).
- 884 73. M. T. Lund, G. Myhre, R. B. Skeie, B. H. Samset, Z. Klimont, Implications of differences  
885 between recent anthropogenic aerosol emission inventories for diagnosed AOD and  
886 radiative forcing from 1990 to 2019. *Atmospheric Chem. Phys.* **23**, 6647–6662 (2023).
- 887 74. T. Knutson, Detection and attribution methodologies overview (APPENDIX C). (2017).

- 888 75. A. Ribes, F. W. Zwiers, J.-M. Azais, P. Naveau, A new statistical approach to climate  
889 change detection and attribution. *Clim. Dyn.* **48**, 367–386 (2017).
- 890 76. Y. Xu, L. Lin, Pattern scaling based projections for precipitation and potential  
891 evapotranspiration: sensitivity to composition of GHGs and aerosols forcing. *Clim. Change*  
892 **140**, 635–647 (2017).
- 893 77. S. Philip, *et al.*, A protocol for probabilistic extreme event attribution analyses. *Adv. Stat.*  
894 *Climatol. Meteorol. Oceanogr.* **6**, 177–203 (2020).
- 895 78. G. J. van Oldenborgh, *et al.*, Pathways and pitfalls in extreme event attribution. *Clim.*  
896 *Change* **166**, 13 (2021).
- 897 79. G. J. Van Oldenborgh, *et al.*, Attributing and Projecting Heatwaves Is Hard: We Can Do  
898 Better. *Earths Future* **10**, e2021EF002271 (2022).
- 899 80. B. Samset, *et al.*, Weak hydrological sensitivity to temperature change over land,  
900 independent of climate forcing. *Npj Clim. Atmospheric Sci.* **1** (2017).
- 901 81. L. J. Wilcox, *et al.*, The Regional Aerosol Model Intercomparison Project (RAMIP).  
902 *Geosci. Model Dev.* **16**, 4451–4479 (2023).
- 903 82. D. Chen, M. Rojas, B. H. Samset, *Chapter 1: Framing, Context and Methods*, 1st Ed.  
904 (Cambridge University Press, 2021).
- 905 83. N. Herger, B. M. Sanderson, R. Knutti, Improved pattern scaling approaches for the use in  
906 climate impact studies. *Geophys. Res. Lett.* **42**, 3486–3494 (2015).
- 907 84. T. D. Mitchell, Pattern Scaling: An Examination of the Accuracy of the Technique for  
908 Describing Future Climates. *Clim. Change* **60**, 217–242 (2003).
- 909 85. B. H. Samset, *et al.*, Climate Impacts From a Removal of Anthropogenic Aerosol  
910 Emissions. *Geophys. Res. Lett.* **45**, 1020–1029 (2018).
- 911 86. G. G. Persad, B. H. Samset, L. J. Wilcox, Aerosols must be included in climate risk  
912 assessments. *Nature* **611**, 662–664 (2022).
- 913 87. R. Schaeffer, *et al.*, Ten new insights in climate science 2024. *One Earth* **8**, 101285 (2025).
- 914 88. M. D. Zelinka, *et al.*, Causes of Higher Climate Sensitivity in CMIP6 Models. *Geophys.*  
915 *Res. Lett.* **47**, e2019GL085782 (2020).
- 916 89. J. Boé, S. Somot, L. Corre, P. Nabat, Large discrepancies in summer climate change over  
917 Europe as projected by global and regional climate models: causes and consequences. *Clim.*  
918 *Dyn.* **54**, 2981–3002 (2020).

- 919 90. S. Seneviratne, X. Zhang, *Climate Change 2021 – The Physical Science Basis: Working*  
920 *Group I Contribution to the Sixth Assessment Report of the Intergovernmental Panel on*  
921 *Climate Change*, 1st Ed. (Cambridge University Press, 2021).
- 922 91. J. Burney, *et al.*, Geographically resolved social cost of anthropogenic emissions  
923 accounting for both direct and climate-mediated effects. *Sci. Adv.* **8**, eabn7307 (2022).
- 924 92. V. Eyring, *et al.*, Overview of the Coupled Model Intercomparison Project Phase 6  
925 (CMIP6) experimental design and organisation. [Preprint] (2015). Available at:  
926 <https://gmd.copernicus.org/preprints/8/10539/2015/gmdd-8-10539-2015.pdf> [Accessed 26  
927 November 2024].
- 928 93. N. Maher, *et al.*, The updated Multi-Model Large Ensemble Archive and the Climate  
929 Variability Diagnostics Package: new tools for the study of climate variability and change.  
930 *Geosci. Model Dev.* **18**, 6341–6365 (2025).
- 931 94. C. Deser, *et al.*, Insights from Earth system model initial-condition large ensembles and  
932 future prospects. *Nat. Clim. Change* **10**, 277–286 (2020).
- 933 95. S. Milinski, N. Maher, D. Olonscheck, How large does a large ensemble need to be? *Earth*  
934 *Syst. Dyn.* **11**, 885–901 (2020).
- 935 96. N. P. Gillett, *et al.*, The Detection and Attribution Model Intercomparison Project (DAMIP  
936 v1.0) contribution to CMIP6. *Geosci. Model Dev.* **9**, 3685–3697 (2016).
- 937 97. N. C. Swart, *et al.*, The Canadian Earth System Model version 5 (CanESM5.0.3). *Geosci.*  
938 *Model Dev.* **12**, 4823–4873 (2019).
- 939 98. G. Danabasoglu, *et al.*, The Community Earth System Model Version 2 (CESM2). *J. Adv.*  
940 *Model. Earth Syst.* **12**, e2019MS001916 (2020).
- 941 99. A. Voltaire, *et al.*, Evaluation of CMIP6 DECK Experiments With CNRM-CM6-1. *J. Adv.*  
942 *Model. Earth Syst.* **11**, 2177–2213 (2019).
- 943 100. O. Boucher, *et al.*, Presentation and Evaluation of the IPSL-CM6A-LR Climate Model. *J.*  
944 *Adv. Model. Earth Syst.* **12**, e2019MS002010 (2020).
- 945 101. H. Tatebe, *et al.*, Description and basic evaluation of simulated mean state, internal  
946 variability, and climate sensitivity in MIROC6. *Geosci. Model Dev.* **12**, 2727–2765 (2019).
- 947 102. I. R. Simpson, *et al.*, The CESM2 Single Forcing Large Ensemble and Comparison to  
948 CESM1: Implications for Experimental Design. *J. Clim.* **1**, 1–53 (2023).
- 949 103. E. Rustemeier, S. Hänsel, P. Finger, U. Schneider, M. Ziese, GPCP Climatology Version  
950 2022 at 1.0°: Monthly Land-Surface Precipitation Climatology for Every Month and the  
951 Total Year from Rain-Gauges built on GTS-based and Historical Data.  
952 [https://doi.org/10.5676/DWD\\_GPCP/CLIM\\_M\\_V2022\\_100](https://doi.org/10.5676/DWD_GPCP/CLIM_M_V2022_100). Deposited 2022.

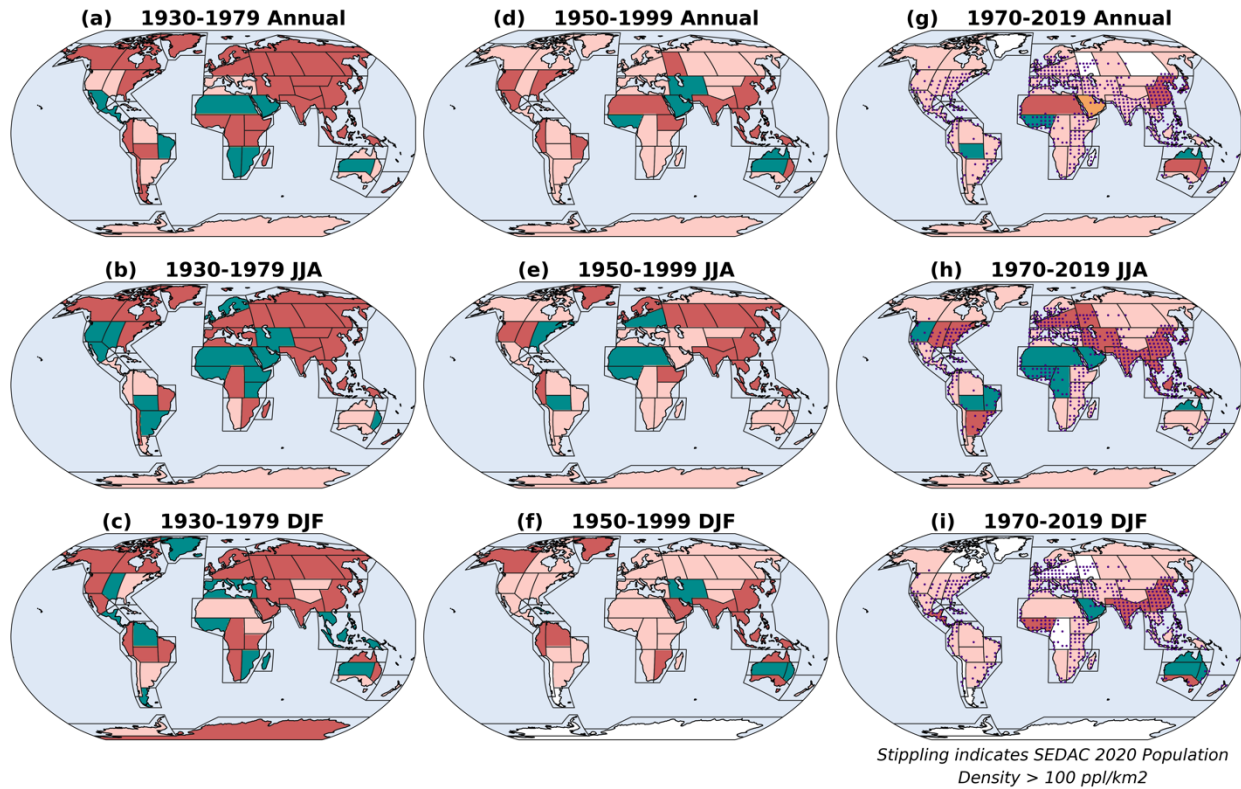
- 953 104. J.-Y. Lee, G. Marotzke, L. Bala, Chapter 4: Future Global Climate: Scenario-based  
954 Projections and Near-term Information. (2021). <https://doi.org/10.1017/9781009157896>.
- 955 105. SEDAC Gridded World Population D... *US Greenh. Gas Cent.* (2025). Available at:  
956 <https://earth.gov/data-catalog/sedac-popdensity-yeargrid5yr-v4.11> [Accessed 18 January  
957 2025].
- 958 106. M. Iturbide, *et al.*, An update of IPCC climate reference regions for subcontinental analysis  
959 of climate model data: definition and aggregated datasets. *Earth Syst. Sci. Data* **12**, 2959–  
960 2970 (2020).
- 961
- 962



963  
964  
965  
966  
967  
968  
969

Figure 1: CESM2 annual-mean aerosol optical depth (AOD) trends for the (a) early (1930-1979), (b) middle (1950-1999), and (c) late (1970-2019) 50-year trend periods. (d) Recent 20-year trend (1995-2014) in Community Emissions Data System (CEDS) version 2017-05-18 SO<sub>2</sub> emissions. Multi-model mean JJA precipitation trends for each 50-year period in ALL (black circle), AER (blue bar), GHG (green bar), and AER+GHG (red square) averaged over (e) Western North America, (f) Eastern North America, (g) Western & Central Europe, (h) Western Africa, (i) Sahara, (j) South Asia, and (k) East Asia. Error bars represent the standard error of the model-mean linear trends. Vertical axes are consistent across (e, f, g, i) and across (h, j, k).

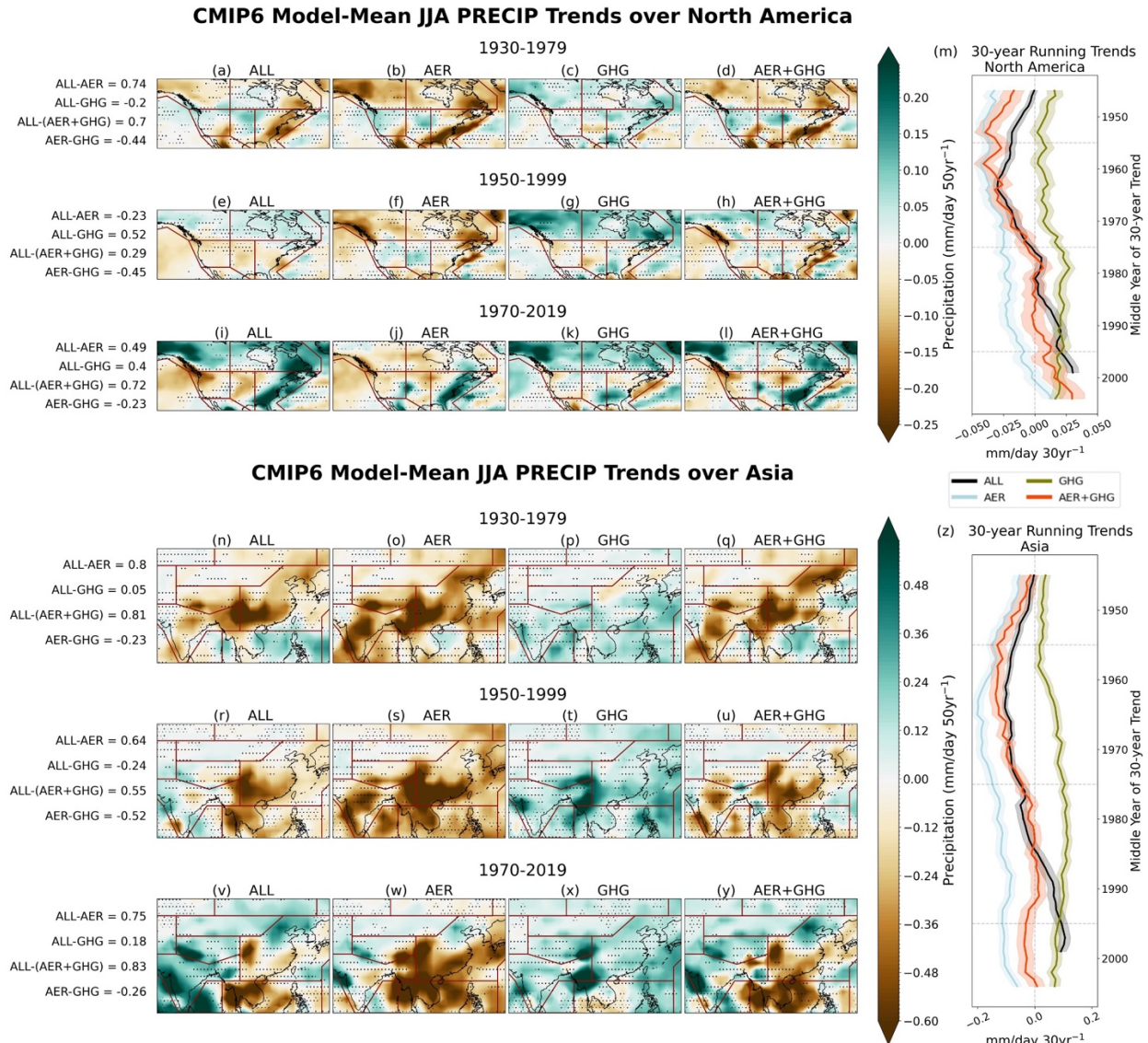
## Dominant AER Contribution to ALL Precipitation Trends (Absolute Trend Contribution)



AER>NONE
  AER>Residual
  AER>GHG
  AER>BOTH and SAME
  AER>BOTH and OPPOSITE

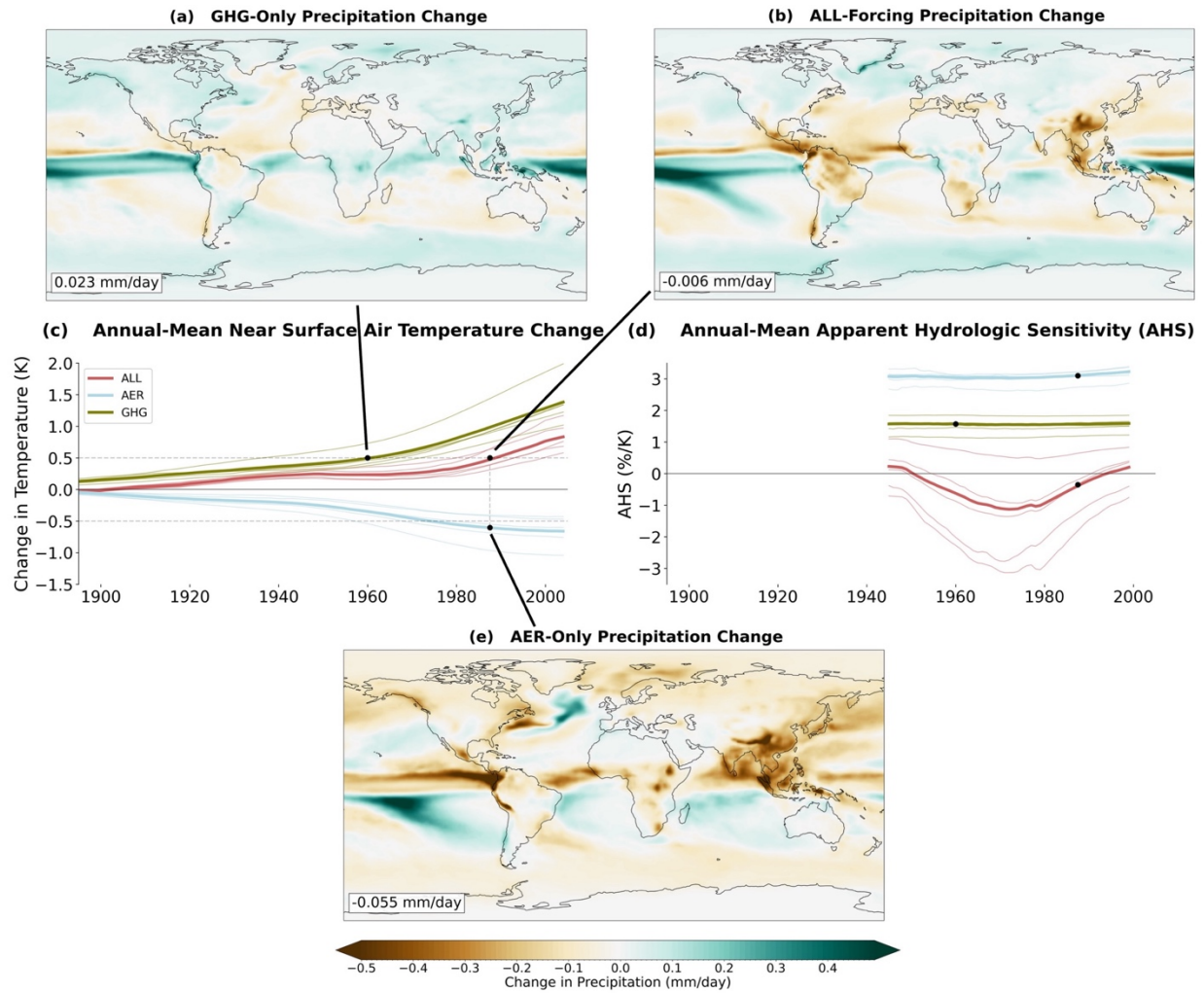
970  
 971  
 972  
 973  
 974  
 975  
 976  
 977  
 978  
 979  
 980  
 981  
 982  
 983  
 984

Figure 2: The spatial-mean absolute contribution to forced historical (ALL) precipitation trends by AER and GHG in the (a, b, c) early, (d, e, f) middle, and (g, h, i) late 50-year periods in the annual-, JJA-, DJF-mean. Regional boundaries are taken from the IPCC AR6 Scientific Regions (106). Regions where AER>NONE (white) highlight where the absolute effect of AER is smaller than both the absolute effect of GHG and the absolute effect of residual natural and anthropogenic forcings [given by ALL – AER+GHG]. Regions where AER>Residual (light pink) highlight where the absolute effect of AER is greater than the absolute effect of residual forcings, but not the absolute effect of GHG. Regions where AER>GHG (orange) highlight where the absolute effect of AER is greater than the absolute effect of GHG, but not the absolute effect of the residual forcings. Regions where AER>BOTH highlight where the absolute effect of AER is greater than the absolute effect of both GHG and residual forcings, distinguishing where AER spatial-mean trends work in the SAME direction as GHG spatial-mean trends (green) and where AER spatial mean trends work in the OPPOSITE direction of GHG spatial-mean trends (red). Grid cells with SEDAC 2020 population density > 100 people/km<sup>2</sup> are shown with stippling in late period (g, h, i). The absolute values of the spatial-mean trends provided in Figure 1e-k are not the values used in the absolute trend calculation in each region in Figure 2, as Figure 2 takes the absolute value prior to the regional-mean. However, the direction of the AER and GHG spatial-mean trend values in Figure 1e-k are responsible for the signal additivity (red vs. green coloring) in Figure 2.



985  
986  
987  
988  
989  
990  
991  
992

Figure 3: LESFMIP multi-model mean ALL, AER, GHG, and AER+GHG JJA precipitation trends over North America in the (a-d) early, (e-h) middle, and (i-l) late 50-year trend periods and Asia in the (n-q) early, (r-u) middle, and (v-y) late 50-year trend periods. Non-stippled regions show regions where four of five models agree on sign of trend. Spatial correlation coefficients between the different pairs of maps are given along the lefthand side. Running 30-year JJA precipitation trends are shown for (m) North America and (z) Asia in ALL (black), AER (blue), GHG (green), and AER+GHG (red); mean values are shown in the colored curves, and the standard error is shown in color shading. Horizontal dashed lines mark the central year of each 50-year trend period shown in the maps.



993  
 994 *Figure 4: Maps show the 30-year model- and annual-mean change in precipitation from the pre-industrial (1850-1880) mean at*  
 995 *a global warming level (GWL) of 0.5 K from (a) GHG (centered around 1960), (b) ALL (centered around 1987), and (e) AER*  
 996 *corresponding to ALL's threshold (centered around 1987). Global-mean values are shown in the lower lefthand corner. Running*  
 997 *30-year annual-mean change in (c) near surface air temperature and (d) apparent hydrological sensitivity (AHS) relative to the*  
 998 *pre-industrial mean (1850-1880) in ALL (red), AER (blue), and GHG (green) are shown. Bolded lines represent model-mean*  
 999 *results and thinner lines represent individual model results. Dashed horizontal lines in (c) represent a global warming level*  
 1000 *(GWL) of +/- 0.5 K. AHS values from 1890-1930 are omitted due to the division of small values during the early 20<sup>th</sup> century.*

1001

1002

### Supplementary Material

1003

Supplementary Material for this manuscript can be viewed and downloaded at

1004

(<https://utexas.box.com/s/prn7tqkwgcmtnceuilma8wp7dyxk0y26>). Supplementary Material

1005

cannot be included in the manuscript draft submission through the *PNAS* portal due to file size

1006

(150MB).